Available online at www.sciencedirect.com
ScienceDirect
Trans. Nonferrous Met. Soc. China 35(2025) 3120−3133

Transactions of
Nonferrous Metals
Society of China
www.tnmsc.cn

Effects of operating parameters on size and distribution of bubbles in coarse-particle flotation column

Ying-sheng JIN[1], Wei SUN[1], Jian PENG[1], Zheng-chang SHEN[2],
Hai-sheng HAN[1], Lei SUN[1], Yao XIAO[1], Yuan-jia LUO[1], Yi CHEN[1]

1. School of Minerals Processing and Bioengineering, Central South University, Changsha 410083, China;
2. State Key Laboratory of Mineral Processing Science and Technology, BGRIMM Technology Group, Beijing 100070, China

Received 25 December 2023; accepted 6 August 2024

Abstract: The size and distribution patterns of bubbles within a laboratory-scale coarse-particle flotation column were examined using a high-speed camera-based dynamic measurement system. The effects of operational parameters such as superficial water velocity, air-flow rate, and frother dosage on bubble-size and distribution characteristics were investigated. This study aims to provide theoretical support for enabling fluidized-bed flotation within coarse-particle flotation columns. The results show that negative pressure for air inspiratory and bubble formation is generated by passing a high-speed jet through a throat, and the greatest number of bubbles are observed under natural inspiratory state at an air−liquid ratio of 1:3−1:2.5. Increasing the air-flow rate transforms the bubble diameter distribution from a peaked distribution to a more uniform distribution. Furthermore, the frother narrows the range of bubble-size distribution. A positive correlation exists between the bubble Sauter diameter and air-flow rate, with the bubble Sauter diameter bearing a negative correlation with the superficial water velocity and frother concentration.

Key words: coarse-particle flotation; fluidized-bed flotation; bubble size; superficial water velocity

---

1 Introduction

Flotation is a versatile and economical concentration method for large-scale mineral processing [1]. This process represents the mass transfer phenomenon involving collision, adhesion, and separation between bubbles and mineral particles [2−6]. During flotation, mineral particles undergo thorough contact and attachment with bubbles to form mineral-bubble aggregates for effective mineral flotation [7]. Bubbles serve as carriers for hydrophobic minerals to froth phase, and bubble characteristics play a critical role in the collision and adhesion of bubbles with particles [8,9]. In flotation, the bubble size directly affects gas holdup, which affects mineralization efficiency, ultimately influencing the grade of the concentrate and its recovery [10]. Consequently, bubbles are a pivotal factor that influences mineral separation.

With declining ore grades and rising ore complexity, the milling cost for valuable metal recovery is increasing [11]. Coarse-particle flotation is important for alleviating the crushing and grinding burden, conserving energy, and reducing consumption [12]. The major challenge in achieving effective coarse-particle flotation is the high probability of particle detachment from the bubble surface [13−16]. The concept of fluidized-bed separation was introduced into the study of flotation columns to overcome the limitations of flotation columns for coarse-particle separation

---

Corresponding author: Jian PENG, Tel: +86-18975869963, +86-13808439573, E-mail: pjiancsu@163.com

https://doi.org/10.1016/S1003-6326(25)66870-1

[17,18]. Fluidized-bed separation combines composite force fields with the flotation phase, thereby considerably reducing the probability of particle detachment from bubbles and effectively increasing the upper limit of the flotation particle size [19−21]. Prominent examples of flotation columns include the NovaCell and HydroFloat cell developed by ERIEZ [1,8,22]. According to AWATEY et al [23,24], the HydroFloat cell can increase the maximum flotation particle size of coarse-grained sphalerite to 1.18 mm, considerably exceeding the separation limit of conventional flotation cells. JAMESON and EMER [25] reported that the use of NovaCell for coarse-particle mineral separation can increase the maximum flotation particle size of galena and chalcopyrite to 1.4 mm. Considering the key technical problems in coarse-particle flotation, we developed a coarse-particle flotation column that integrates turbulent mineralization, steady flow transition, and static sorting zones to provide an optimal flow field environment for flotation. The application of fluidization technology considerably reduces the resistance to the flotation of coarse particles, and the introduction of microbubble generation technology to the flotation and separation process helps generate a bubble cluster that is suitable for the flotation of coarse particles.

The operating parameters in fluidized-bed flotation columns, such as rising water rate, air volume, and frother dosage, have different degrees of impact on the bubble size and distribution, thereby influencing the flotation performance. PANJIPOUR et al [26] explored the correlation among bubble-size distribution, gas holdup, bubble interfacial area, and flotation kinetics by manipulating variables such as the air-flow rate and frother dosage. Their results suggest that gaining an understanding of the bubble-size distribution is necessary for demonstrating flotation kinetics under different flotation conditions. XU et al [27] used the photographic method and MATLAB software to investigate the effects of operating parameters, such as circulating pressure, air-filling volume, and frother, on bubble size in flotation columns. Experimental data and image analyses showed that the amount of frother and the degree of inflation greatly affected bubble size. In coarse-particle flotation, the upward flotation of coarse particles depends on the drag force of the rising water flow to reduce the probability of detachment of coarse particles and to increase the adhesion degree of particles to the bubbles [28,29]. At present, there is a lack of research on the effect of rising water flow on the size and distribution of bubbles.

Herein, we used a self-developed coarse-particle flotation column and incorporated sampling tubes within an observation chamber to visualize bubbles within the fluidized flotation column. We adopted high-speed photogrammetry and other techniques to establish a dynamic bubble-size measurement system. This allowed us to capture image data depicting bubble-size distribution within the flotation column. Subsequently, we processed the data using Python code to compile extensive statistics on bubble size from the image dataset. The effects of the operating parameters on the bubble-size distribution and dimensions in the flotation column were thoroughly analyzed. Furthermore, we observed the correlation between the bubble Sauter diameter and the operating parameters through data fitting. This study on bubble size and distribution makes contribution to improving coarse-particle separation efficiency and offers theoretical support for advancing coarse-particle flotation columns.

2 Experimental

2.1 Experimental design and test methods

Figure 1 presents a schematic of the bubble size measurement system. A feed tube was arranged in the upper part of the coarse-particle flotation column. From bottom to top, the column was divided into a bottom flow trough, a swirl mineralization area, and a static separation area. A water−gas mixed jet tube was arranged on the side wall of the swirl mineralization area. The jet direction was distributed clockwise or counterclockwise, with the axis of the flotation column as the center. A damping element was also arranged between the swirl mineralization zone and the static separation zone to reduce flow turbulence. The damping elements were distributed equidistantly around the inner wall of the flotation column. The water−gas mixing cavitation bubble system comprised a water supply part, a gas supply part, and a water−gas mixing bubbler. The gas required by the coarse-particle flotation column was supplied by an air compressor. A pressure gauge was used to regulate the pressure of the gas. Further, a glass rotameter was used to adjust the suction volume. Subsequently, the air was fed into the bubbler at a certain pressure and flow rate. The water tank was filled with 3 L of water, and the frother was added according to the test conditions. Then, water was fed into the bubbler using a peristaltic pump. Due to the jet action in the bubbler, the gas was dispersed into fine bubbles and entered the coarse-particle flotation column along with water as a mixed fluid. The bubble observation chamber was filled with the same deionized water or with the same concentration of frother solution as that in the coarse-particle flotation column. The observation chamber was then inverted and held over the mouth of the column during the experiment. A bubble collection tube was positioned atop the flotation column. This tube had a sufficiently large inner diameter to prevent compression and other unfavorable effects during bubble-size measurement.

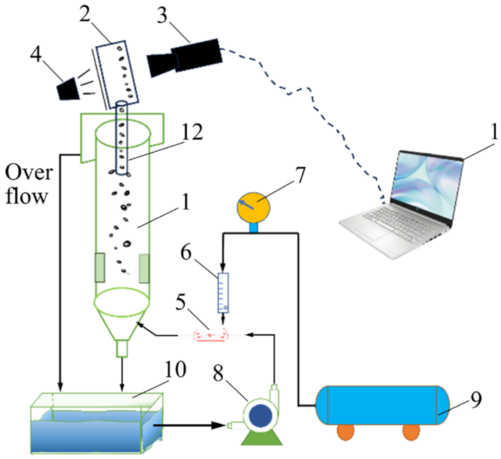

Fig. 1 Measurement system schematic of bubble size: 1−Coarse-particle flotation column; 2−Bubble-sampling observation room; 3−High-speed camera; 4−Light-emitting diode; 5−Frothing generator device; 6−Flowmeter; 7−Pressure gage; 8−Peristaltic pump; 9−Air compressor; 10−Tank; 11−Computer; 12−Bubble collection tube

Figure 2 shows a schematic of the system for bubble sampling and the high-speed camera system. The observation room was 100 mm × 50 mm × 20 mm. The chamber had openings at the top and bottom. The bottom part of the chamber was connected to the sampling tube through a rubber plug, and the top part was connected to the water reservoir through a rubber hose. In this system, the sampling tube had an inner diameter of 10 mm and an outer diameter of 14 mm. The camera system comprised a white light emitting diode as the light source and a Nikon F-Mount YA-860 high-speed camera. The system was designed to study the motion behavior of the bubble population, measure the bubble-size distribution inside the flotation column, and investigate the diffusion pattern of the bubbles inside the coarser particle flotation column.

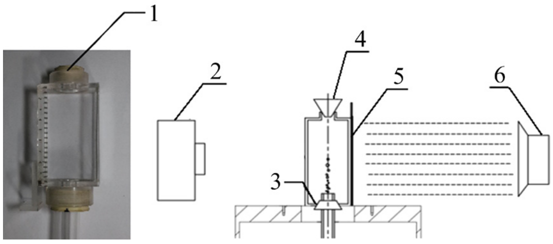

Fig. 2 Schematic of bubble sampling and high-speed camera system: 1−Object of observation room; 2−High-speed camera; 3, 4−Rubber sealing plug; 5−Scale plate; 6−Parallel light source

2.2 Measurement of bubble size

Deionized water was used and the tests were conducted at room temperature (23 °C). To facilitate the comparison of the effect of test conditions on the bubble size, 3000 bubble pictures were processed equally for each test condition.

First, the column was filled with water and the peristaltic pump was started. Then, the bubble observation chamber was filled with the same liquid phase as that inside the column. The sampling tube was inserted at the measurement position and held there for 2 min. The bubble generator valve was opened or the compressed air machine was started, and the air flow was adjusted using a glass rotor flow meter and control valve. Simultaneously, the illumination source (parallel light) was turned on and the camera took 3000 pictures continuously at a frequency of 200 fps. Subsequently, the pictures were converted to MPG format using the MotionBLITZ Director2 software of the high-speed camera. The bubble images obtained from the experimental photography were then processed using Python interface code in the open-source computer vision software library OpenCV.

Figure 3 depicts the transformation of the image using the Python third-party matrix computation library NumPy. We first used the

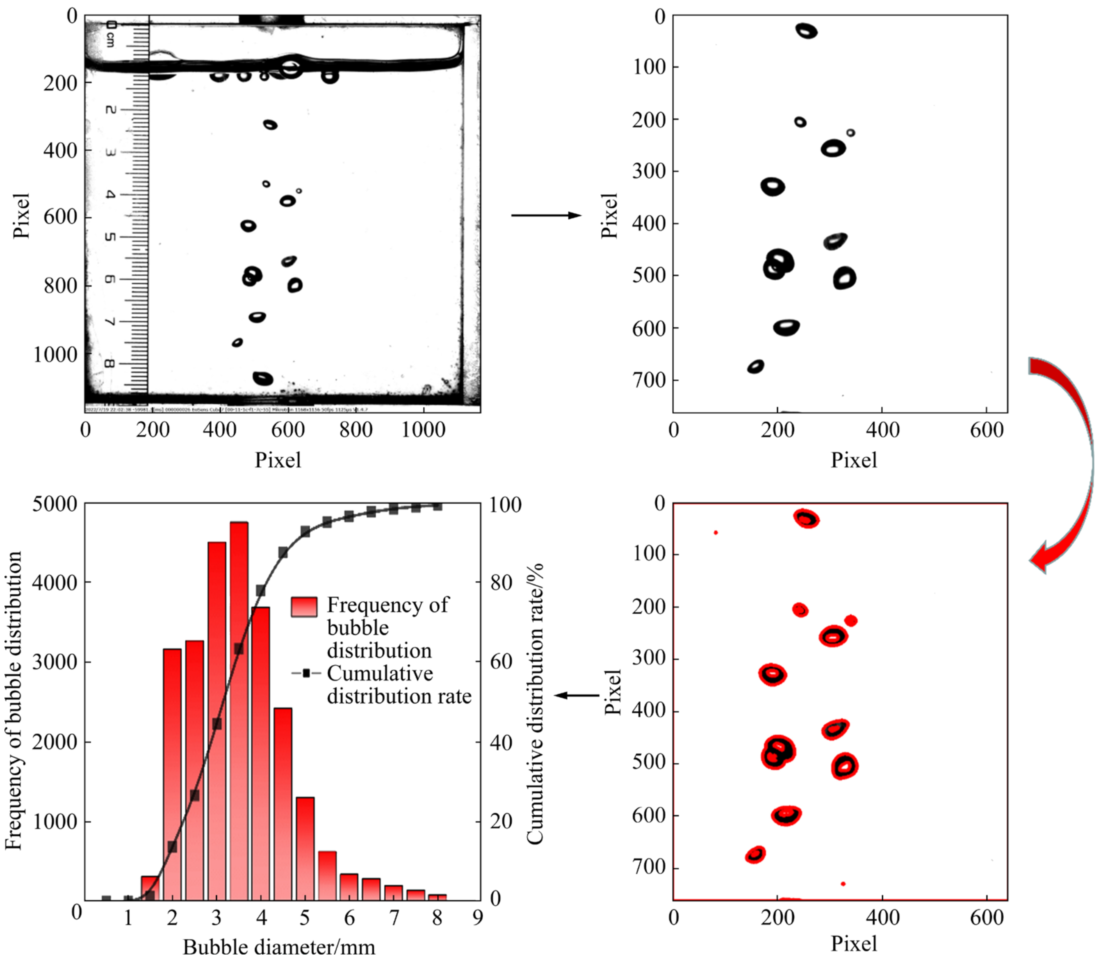

Fig. 3 Measurement and analysis of bubble size distribution

cv2.cvtColor function to transform the image from the RGB space to the grayscale space and then used the cv2.threshold function to binarize the grayscale image to distinguish foreground bubble contours and irrelevant backgrounds. Subsequently, we used the cv2.findContours function to defect all contours in the binarized image. Finally, we used the cv2.contourArea function and cv2.arcLength to calculate the pixel area and pixel perimeter of the bubble, respectively, as well as to obtain the actual bubble size based on the proportionality between the image and the actual bubbles.

2.3 Bubble Sauter diameter

The Sauter diameter was used to describe the average size of the bubble cluster. The diameter is calculated as

$$d_{32}=\frac{\sum n_i d_i^3}{\sum n_i d_i^2} \tag{1}$$

where d_{32} represents the Sauter diameter of the bubble population, d_i represents the diameter of the ith bubble, and n_i represents the number of bubbles with diameter d_i. Using the Sauter diameter, the average diameter of the bubble population can be obtained under specific experimental conditions.

2.4 Surface tension measurement

The surface tension of solutions with varying concentrations of the frothing agent, i.e., methyl isobutyl carbinol (MIBC), was experimentally measured. The MIBC used in the experiments had chemical purity, with a relative molecular mass of 102.17. It was supplied by Aladdin Corporation. Several MIBC solutions with a concentration gradient were prepared, and the surface tension was then tested on a comprehensive surface tension tester (BZY-2, Shanghai Hengping Instrument Co., Ltd., China). The testing was performed at room temperature. Three tests were conducted for each set of tests, and the average was taken as the final result.

3 Results and discussion

3.1 Superficial water velocity

3.1.1 Effects on bubble size

As shown in Figs. 4 and 5, the bubble diameters are mainly concentrated in the range of 2−4.5 mm under different test conditions, and the bubble contents outside this range are relatively low, which almost shows a normal distribution. At the superficial gas velocity (Q_g) of 0.05 m^3/h, with an increase in superficial water velocity, the bubble diameter distribution and number of bubbles demonstrate certain regularity. In Fig. 5(a), the superficial water velocity (Q_l) is 0.09 m^3/h, the ratio of the filling volume and superficial water velocity (hereinafter, the gas−liquid ratio) is 1∶1.8, and the number of bubbles with intermediate sizes of 2−4.5 mm is relatively close to the number of bubbles with intermediate grain size in 3000 pictures, and the average is ~2300 in the middle. With increasing water velocity, when the gas−liquid ratio increased from 1∶1.8 to 1∶2.4, the frequency of bubbles with the intermediate size of 2−4.5 mm tended to increase while that of large bubbles in the range of 4.5−8 mm tended to decrease. When the gas–liquid ratio was 1∶3 (Fig. 5(c)), the number of bubbles increased overall; in particular, the frequency of bubbles having an intermediate size continued to show an increasing trend and the number of bubbles with size ~3 mm reached 4500. However, the overall number of bubbles did not continue to increase when the amount of rising water increased to a certain degree (Fig. 5(d)). When the gas–liquid ratio was 1∶4.2, the number of bubbles within the range of 3.5−4 mm decreased while that of bubbles within the range of 2−2.5 mm increased; the peak of the number of bubbles shifted in the direction of the small bubbles.

The reason for this peak shift can be explained as follows. Within the bubble generator and the coarse-particle flotation column, bubbles undergo coalescence and breakup. Under constant superficial gas velocity, when the rising water rate is low, the energy acquired per unit of gas is minimal. Therefore, larger bubbles are prevalent

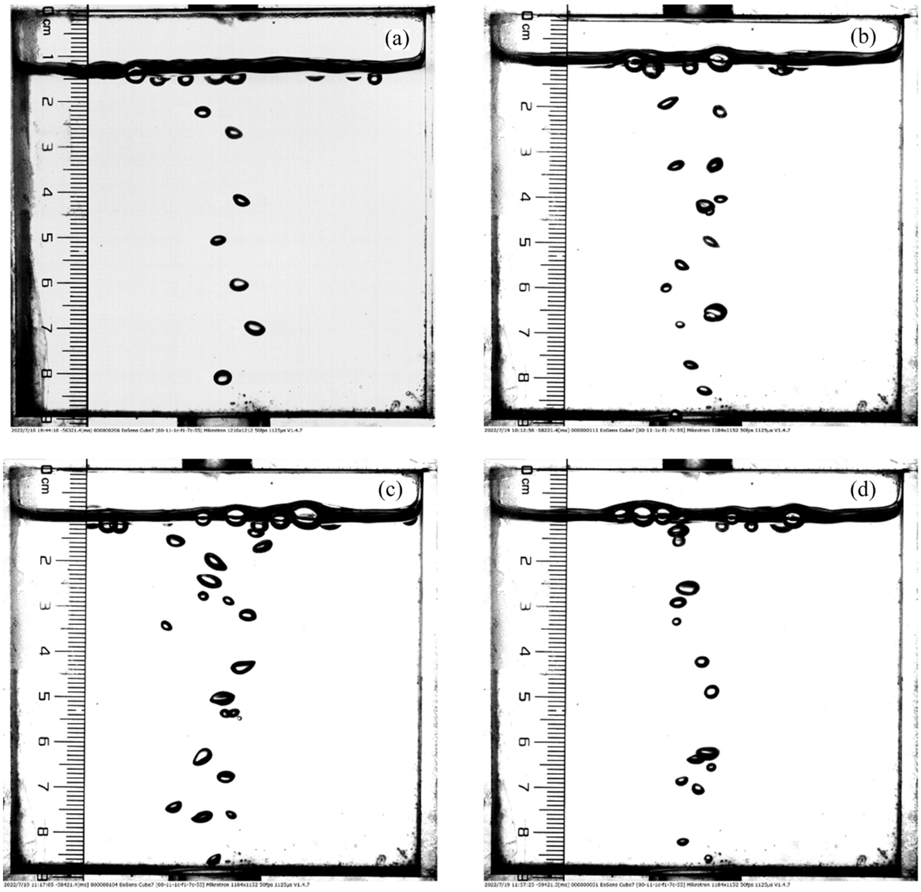

Fig. 4 Original images of bubble size at different superficial water velocities (Q_g=0.05 m^3/h): (a) Q_l=0.09 m^3/h; (b) Q_l= 0.12 m^3/h; (c) Q_l=0.15 m^3/h; (d) Q_l=0.21 m^3/h)

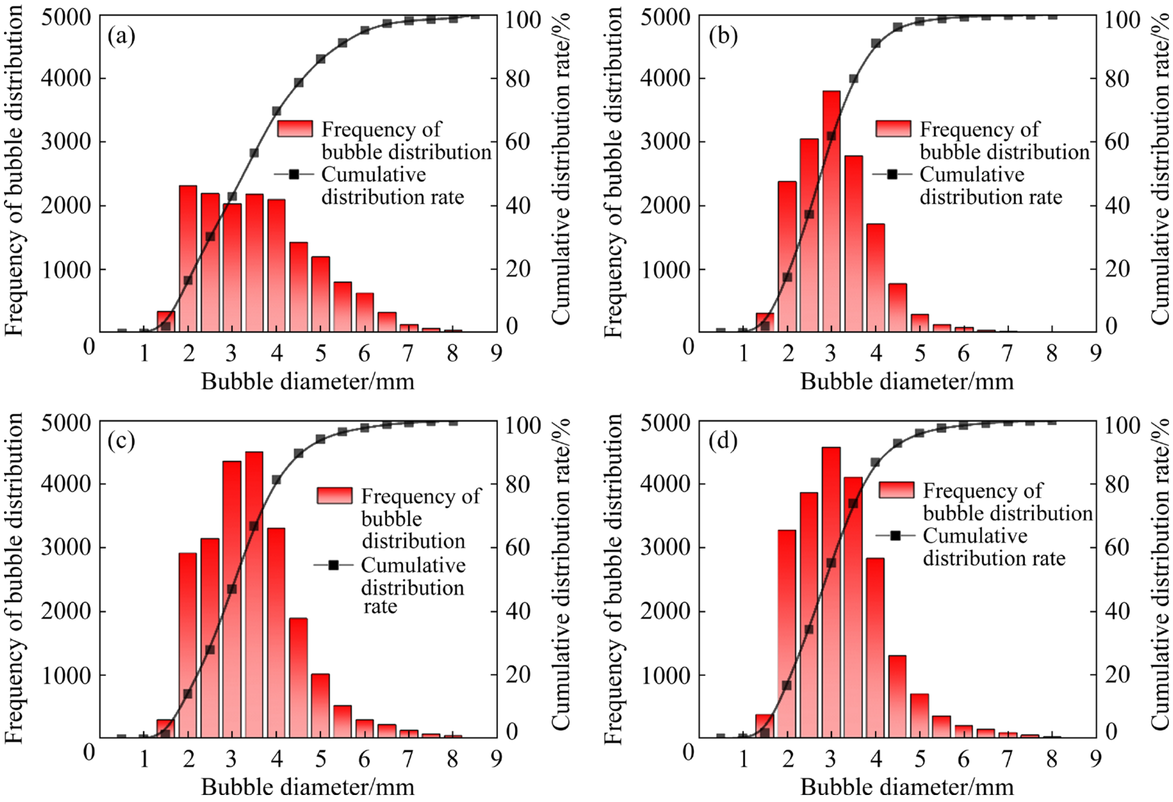

Fig. 5 Bubble size and distribution at different superficial water velocities (Q_g=0.05 m^3/h): (a) Q_l=0.09 m^3/h; (b) Q_l= 0.12 m^3/h; (c) Q_l=0.15 m^3/h; (d) Q_l=0.21 m^3/h

because the coalescence rate is greater than the breakup rate. As the superficial water velocity increases, the energy acquired per unit of gas also increases. At this point, the bubble breakup rate exceeds the coalescence rate, increasing the number of bubbles. When this increase reaches a certain threshold, the peak of the number of bubbles shifts toward smaller bubbles.

3.1.2 Trend in bubble distribution changes

The probability density distribution of bubble sizes and their fitting results at an superficial gas velocity of 0.05 m^3/h and superficial water velocities of 0.09, 0.12, 0.15, and 0.21 m^3/h are shown in Fig. 6, and the corresponding R^2 values for the fitted lognormal distribution functions, as listed in Table 1, are 0.934, 0.982, 0.958, 0.959 and 0.975 respectively, indicating a good fit.

Currently, the Sauter diameter is widely used globally to characterize the average size of a bubble system. Using Eq. (1), calculations were performed to determine the Sauter diameter of the bubbles in various experimental conditions. Subsequently, curves of the Sauter diameter were generated to illustrate the effect of changing rising water rates. As shown in Fig. 7, the Sauter diameter of the bubbles decreases with increasing water rates. Furthermore, a notable inflection point was observed under natural aspiration conditions.

3.2 Superficial gas velocity

3.2.1 Effects on bubble size

As shown in Figs. 8 and 9, under a constant rising water rate of 0.15 m^3/h but varying superficial gas velocities, many bubbles of intermediate sizes (2−4.5 mm) are present. However, there are distinct differences in the histograms depicting the distribution of bubble diameters. In Fig. 9(a), for a gas−liquid ratio of 1:6, there are ~5000 bubbles with an intermediate size of 2.5 mm. As the superficial gas velocity increases, corresponding to a change in the gas–liquid ratio from 1:6 to 1:3, the frequency of bubbles in the size range of 2–3 mm shows a declining trend, whereas that of large bubbles (3.5–5 mm) increases. With further increase in the superficial gas velocity, resulting in a gas−liquid ratio of 1:2.5, high-speed jets pass through a nozzle to create a negative pressure and introduce air to generate bubbles.

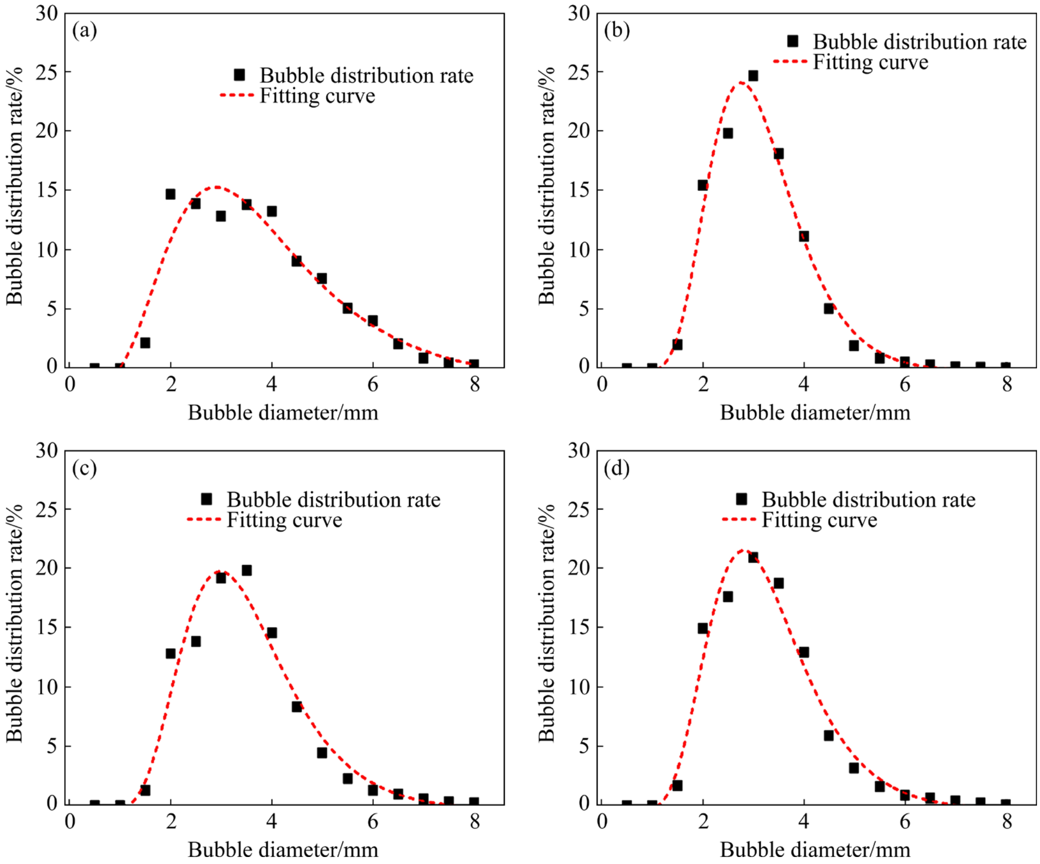

Fig. 6 Fitting curves of bubble size distribution at different superficial water velocities (Q_g=0.05 m^3/h): (a) Q_l=0.09 m^3/h; (b) Q_l=0.12 m^3/h; (c) Q_l=0.15 m^3/h; (d) Q_l=0.21 m^3/h

Table 1 Parameters obtained by fitting using lognormal distribution

Operating parameter			Fitting parameter				
Superficial gas velocity/(m^3·h^{-1})	Superficial water velocity/(m^3·h^{-1})	Frother dosage/(mg·L^{-1})	μ/mm	σ	Expected value	Variance	R^2
0.05	0.09	0	3.581	0.463	3.987	1.951	0.934
0.05	0.12	0	3.013	0.297	3.149	0.957	0.982
0.05	0.15	0	3.334	0.335	3.526	1.214	0.958
0.05	0.18	0	3.287	0.357	3.504	1.293	0.959
0.05	0.21	0	3.125	0.326	3.295	1.103	0.975

μ: Average of bubble size; σ: Standard deviation

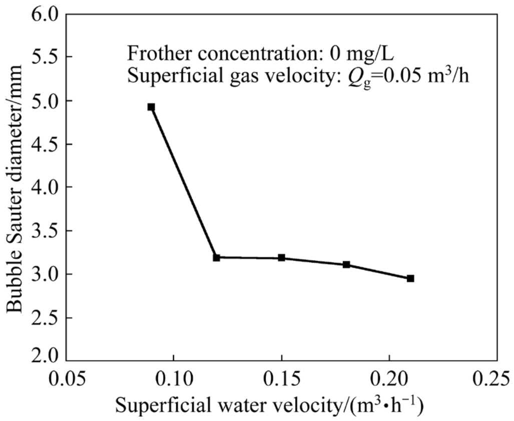

Fig. 7 Distribution of bubble Sauter diameter at different superficial water velocities

According to the working principle of the Venturi tube bubble generator, this device operates under natural aspiration when no additional air is introduced by the air compressor. If the gas–liquid ratio exceeds 1:2.5, the air compressor is used to supplement the gas to the bubble generator. The conditions shown in Figs. 9(c) and (d) represent cases where additional gas was supplied. Figure 9(b) illustrates that under natural aspiration conditions, the overall quantity of bubbles reaches a maximum. Under a constantly superficial water velocity of 0.15 m^3/h, as the superficial gas velocity increases and the gas–liquid ratio exceeds the value of natural

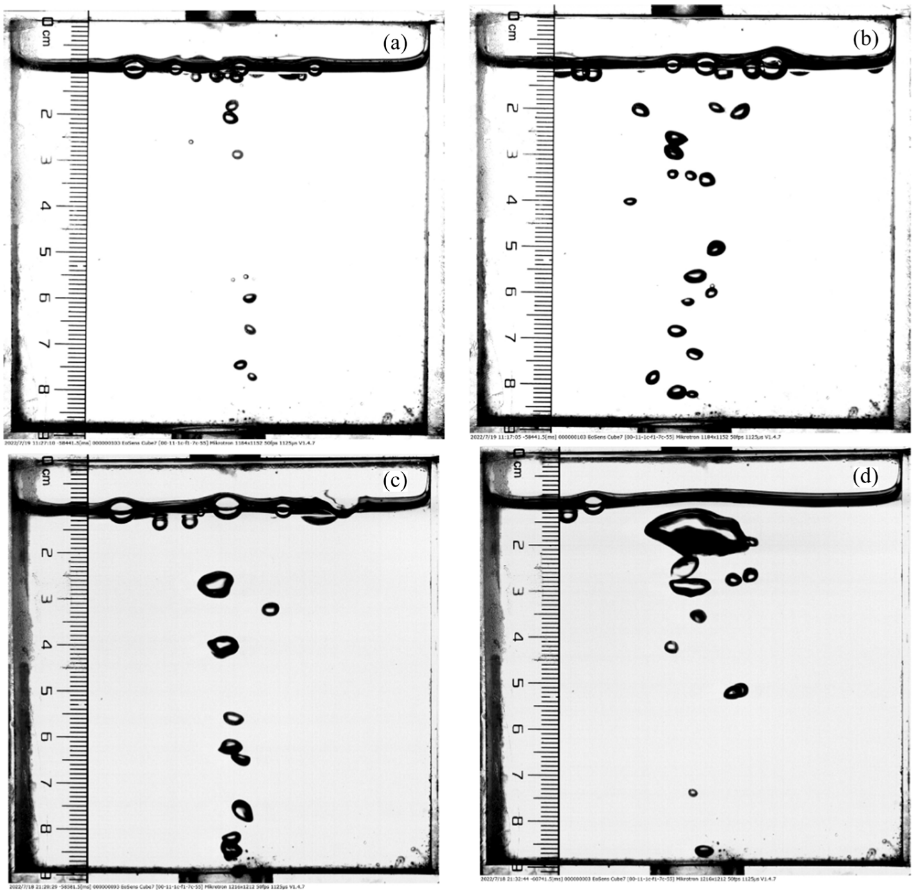

Fig. 8 Original images of bubble size at different superficial gas velocities (Q_l=0.15 m^3/h): (a) Q_g=0.025 m^3/h; (b) Q_g=0.06 m^3/h; (c) Q_g=0.075 m^3/h; (d) Q_g=0.125 m^3/h

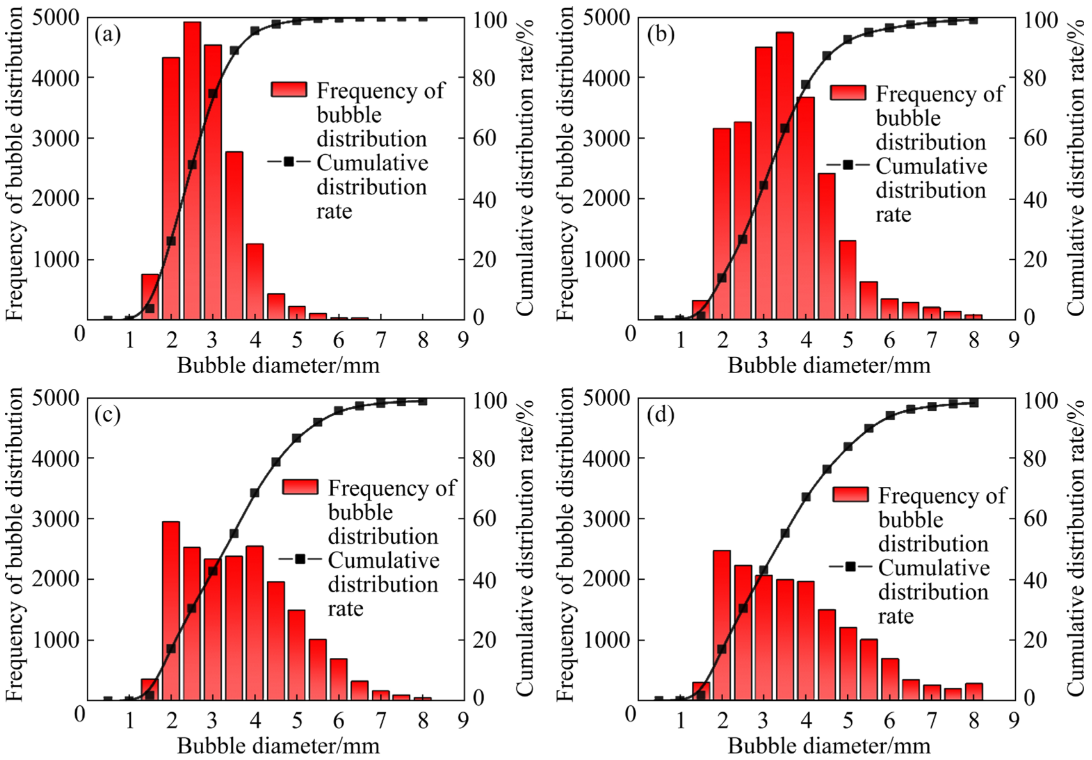

Fig. 9 Bubble size and distribution at different superficial gas velocities (Q_l=0.15 m^3/h): (a) Q_g=0.025 m^3/h; (b) Q_g=0.06 m^3/h; (c) Q_g=0.075 m^3/h; (d) Q_g=0.125 m^3/h

aspiration, the bubble diameter distribution shifts from a sharp peak to a flatter peak, accompanied by a decrease in the number of bubbles. In Fig. 9(d), the number of bubbles in the intermediate size range of 2−4.5 mm decreases to ~2300.

Under the conditions of a constantly superficial water velocity, when the superficial gas velocity is relatively low and the gas–liquid ratio is less than that under natural aspiration, the energy obtained by a unit of gas for lifting water is higher. In this scenario, the bubble breakage rate exceeds the coalescence rate, resulting in an increase in the number of bubbles. Meanwhile, when the superficial gas velocity surpasses the gas−liquid ratio under natural aspiration, the turbulence intensity around the bubble changes [30,31]. And a substantial amount of gas experiences intense collisions within the bubble generator and the coarse-particle flotation column. When the kinetic energy from these collisions exceeds the hydration film between the bubbles, the bubbles coalesce. At this point, the coalescence rate surpasses the breakage rate, increasing the number of large bubbles. However, the number of bubbles decreases.

3.2.2 Trend in bubble distribution changes

Figure 10 shows the probability density distribution of bubble sizes and their fitting curves corresponding to a superficial water velocity of 0.15 m^3/h and superficial gas velocities of 0.025, 0.05, 0.075, 0.10 and 0.125 m^3/h; the corresponding fitting R^2 values for the logarithmic normal distribution functions are 0.990, 0.958, 0.908, 0.902 and 0.914, respectively (Table 2). These values indicate a gradual decrease in the fitting quality as the superficial gas velocity increases. As shown in Fig. 11, the Sauter diameter of the bubbles increases at a high superficial gas velocity. Notably, this figure shows a distinct inflection point that also occurs under conditions of natural aspiration.

3.3 Frother

3.3.1 Effects on bubble size

When the superficial water velocity and superficial gas velocity are kept constant and the dosage of the frother is varied, the histograms of the bubble diameter distribution shown in Fig. 12 show that the bubble diameter distribution is primarily concentrated around intermediate-sized bubbles.

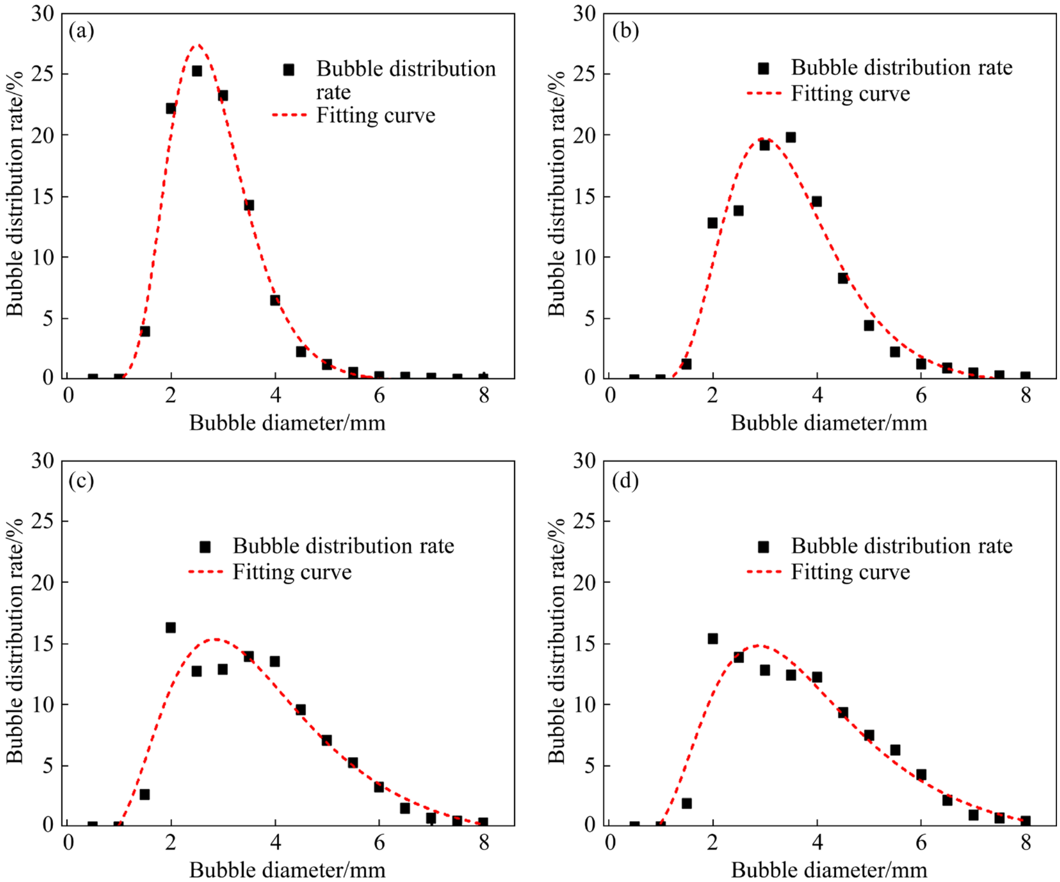

Fig. 10 Fitting curves of bubble size distribution at different superficial gas velocities (Q_l=0.15 m^3/h): (a) Q_g=0.025 m^3/h; (b) Q_g=0.06 m^3/h; (c) Q_g=0.075 m^3/h; (d) Q_g=0.125 m^3/h

Table 2 Parameters obtained by fitting using lognormal distribution

Operating parameter			Fitting parameter				
Superficial gas velocity/($m^3\cdot h^{-1}$)	Superficial water velocity/($m^3\cdot h^{-1}$)	Frother dosage/ ($mg\cdot L^{-1}$)	μ/mm	σ	Expected value	Variance	R^2
0.025	0.15	0	2.709	0.286	2.822	0.824	0.990
0.05	0.15	0	3.334	0.335	3.526	1.214	0.958
0.075	0.15	0	3.559	0.475	3.984	2.004	0.908
0.10	0.15	0	3.641	0.481	4.087	2.086	0.902
0.125	0.15	0	3.611	0.480	4.053	2.065	0.914

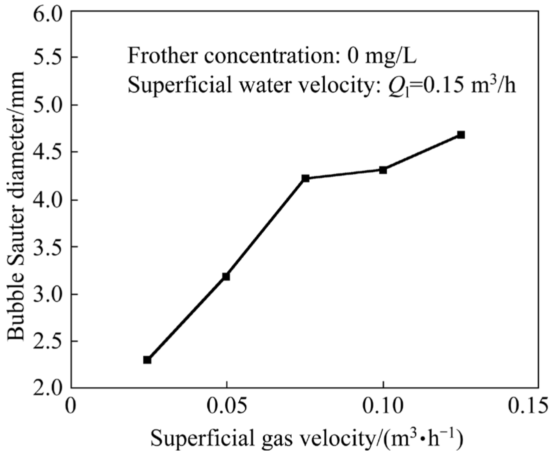

Fig. 11 Bubble Sauter diameter at different superficial gas velocities

There are relatively few bubbles on both sides of the peak, and the distribution approximates a normal distribution. When the frother is absent, the distribution range of bubble sizes is broad and the histogram of bubble distribution exhibits a bimodal feature, indicating a high number of bubbles in two size ranges, with the primary bubble diameter size distribution between 2 and 4.5 mm. As the dosage of the frother is increased, the maximum bubble diameter and the range of diameter distribution substantially decrease. Simultaneously, the peak of the bubble distribution histogram strengthens. The number of large bubbles decreases, whereas that of small bubbles increases, leading to a gradual concentration of the bubble distribution. For instance, at a frother concentration of 2.5 mg/L, the bubble size distribution is concentrated between 0.5 and 1.5 mm. When the frother concentration is further increased to 5.0 mg/L, the bubble size distribution is concentrated between 0.3 and 1.0 mm. Furthermore, the bubble diameter corresponding to the peak of the bubble distribution rate decreases with an increase in the concentration of the frother, further confirming that the bubble size is reduced at high concentrations of the frother. As shown in

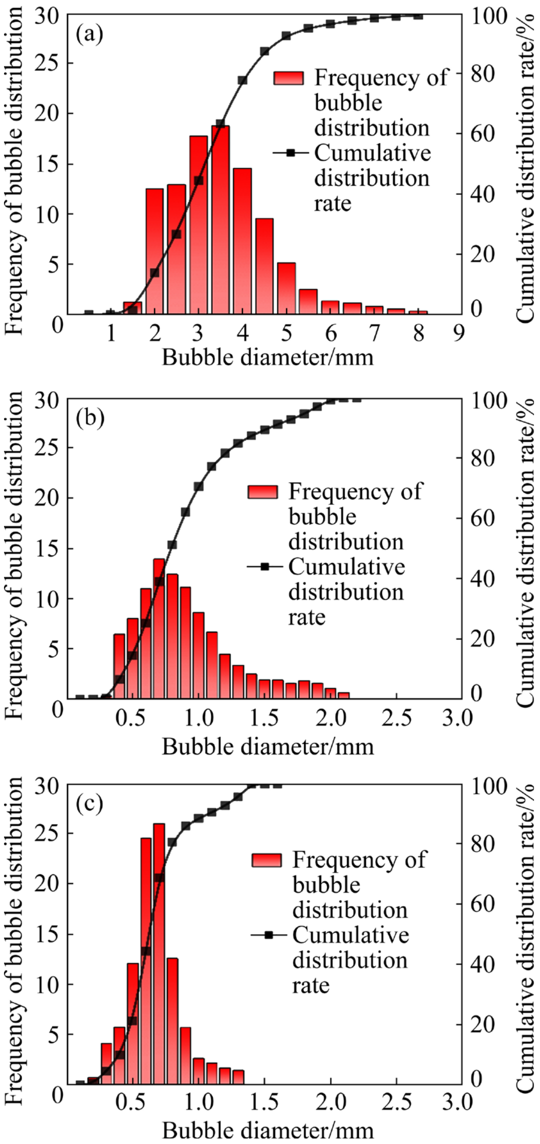

Fig. 12 Bubble size distribution at different concentrations of frother (natural inspiratory state: Q_l= 0.15 m³/h, and Q_g=0.06 m³/h): (a) 0 mg/L; (b) 2.5 mg/L; (c) 5 mg/L

Fig. 12, in the absence of frother, the maximum bubble size is 7.5 mm. At frother concentrations of 2.5 and 5 mg/L, the maximum bubble sizes are 2.2 and 1.4 mm, respectively.

This observed pattern can be explained as follows: MIBC is an alcohol-based frother. Its molecular structure contains hydroxyl groups (—OH), which can form strong hydrogen bonds with water molecules. When MIBC molecules are introduced into water, they inhibit the coalescence of bubbles. After the liquid film between the bubbles is strengthened, the bubbles must overcome a larger surface energy barrier to coalesce, thus making the bubbles more stable. It is worth noting that the addition of MIBC can reduce the bubble size. Because MIBC stands upright at the air–water interface, the —OH group faces the water phase and the hydrophobic chain faces the air phase [32]. The formation of a single layer of MIBC molecules at the gas–liquid interface limits the expansion of the bubbles, resulting in a more uniform bubble size.

This phenomenon can be explained by considering another perspective. DUINEVELD [33] introduced the Weber coefficient, W_e, to quantify the conditions for merging bubbles as follows:

$$W_e=\frac{\rho_l V_{av}^2}{2\gamma}\times\left(\frac{1}{r_{b1}}+\frac{1}{r_{b2}}\right) \tag{2}$$

where ρ_l is the density of liquid, r_{b1} and r_{b2} represent the diameters of bubbles 1 and 2, respectively, and V_{av} represents the relative velocity of the bubbles. As shown in Fig. 13, the results indicate that when W_e exceeds the threshold value (W_{cc}), bubbles 1 and 2 experience the collision and rebound phenomena. However, if this threshold is not reached, the bubbles will coalesce. Adsorption of the frother on the bubble reduces the surface tension of the bubbles. Based on Eq. (2), as surface tension decreases, W_e increases. When W_e exceeds W_{cc}, the coalescence ability of the bubbles weakens, leading to a reduction in the bubble diameter.

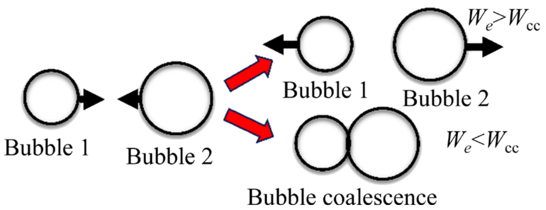

Fig. 13 Collision, coalescence, and separation of bubbles

3.3.2 Trend in bubble distribution changes

The bubble size distributions of MIBC at different concentrations were compared experimentally. The probability density distribution of bubble sizes and the fitting results with R^2 values of 0.955, 0.975, and 0.969 are shown in Fig. 14. The data in Table 3 indicate that the expectation and variance of bubble sizes decrease with the increasing concentration of the frother. This result indicates a trend of reducing average bubble size and increasing bubble uniformity. Figure 15 shows a considerable reduction in the Sauter diameter of

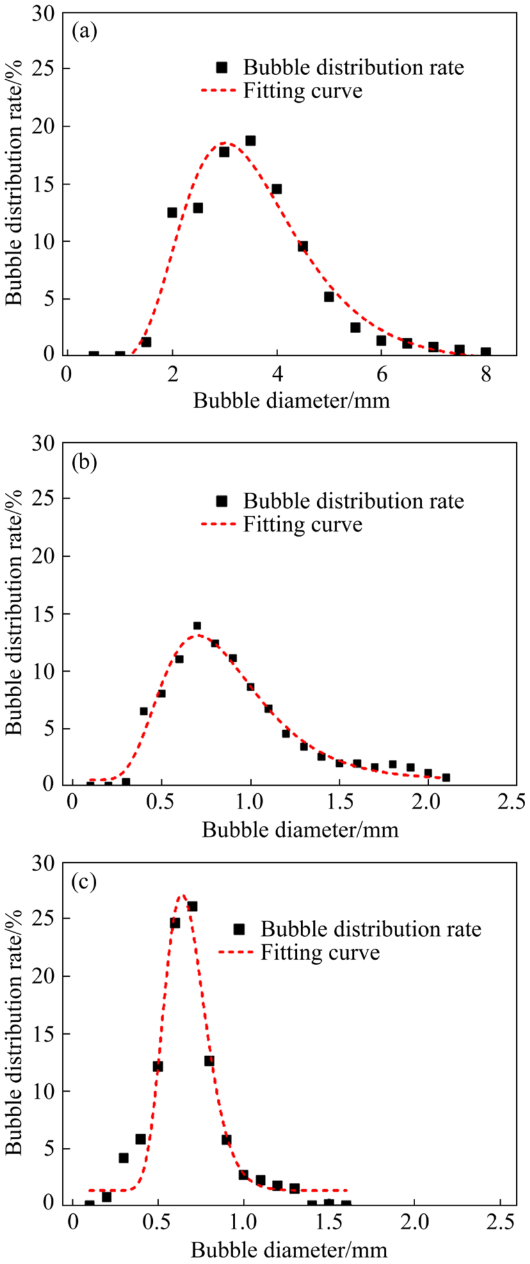

Fig. 14 Fitting curves of bubble size distributions for different dosages of frother: (a) 0 mg/L; (b) 2.5 mg/L; (c) 5 mg/L

Table 3 Parameters obtained by fitting with lognormal distribution

Operating parameter			Fitting parameter				
Superficial gas velocity/($m^3 \cdot h^{-1}$)	Superficial water velocity/($m^3 \cdot h^{-1}$)	Frother dosage/($mg \cdot L^{-1}$)	μ/mm	σ	Expected value	Variance	R^2
0.06	0.15	0	3.405	0.350	3.620	1.307	0.955
0.06	0.15	2.5	0.810	0.376	0.870	0.339	0.975
0.06	0.15	5	0.662	0.187	0.673	0.127	0.969

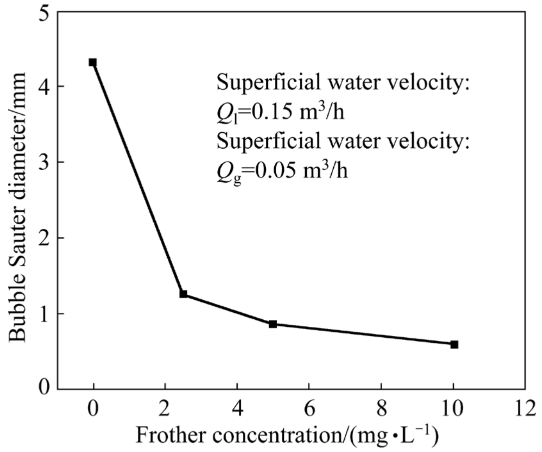

Fig. 15 Sauter diameter of bubbles for different concentrations of frother

bubbles after the addition of a small amount of frother. This reduction is attributed to the decrease in the surface tension of the system because of the addition of the frother, which effectively inhibits the coalescence among bubbles. Furthermore, as the concentration of the frother continues to increase, the reduction of the Sauter diameter of the bubbles becomes less pronounced because of the increased elasticity of the gas−liquid interface in the liquid phase with further increase in the frother concentration.

4 Conclusions

(1) Air is drawn in and bubbles are generated using a high-speed jet through a nozzle to create negative pressure. Under natural aspiration, the gas−liquid ratio is in the range of 1:2.5−1:3, and in this range, the bubble count reaches its peak. As the air injection rate gradually increases, the bubble size distribution changes from a peaked shape to a flatter profile, with a continuous increase in the number of larger bubbles; however, the overall bubble count begins to decrease. Furthermore, the addition of the frother considerably narrows the range of bubble size distribution and reduces the average bubble size.

(2) The lognormal distribution function provides a more precise representation of the distribution pattern of bubble size in the coarse-grained flotation column. The results indicate that with an increase in the frother concentration, the mean and variance of the bubble size distribution decrease. This results in a significant reduction in the average bubble size and an improvement in the uniformity of the bubble distribution.

(3) The Sauter diameter of bubbles decreases with an increase in the superficial water velocity and exhibits an increasing trend with an increase in the air-flow rate. After adding a certain amount of the frother, there is a substantial increase in the reduction of the Sauter diameter of bubbles. However, with a further increase in the frother concentration, the magnitude of the reduction in the Sauter diameter of bubbles gradually decreases.

CRediT authorship contribution statement

Ying-sheng JIN: Conceptualization, Investigation, Methodology, Formal analysis, Writing − Original draft; **Wei SUN:** Methodology, Data curation; **Jian PENG:** Investigation, Software, Writing − Original draft; **Zheng-chang SHEN:** Methodology, Resources; **Hai-sheng HAN:** Writing − Review & editing; **Lei SUN:** Supervision, Methodology; **Yao XIAO:** Investigation; **Yuan-jia LUO:** Resources; **Yi CHEN:** Investigation, Methodology.

Declaration of competing interest

The authors declare that they have no known competing financial interests or personal relationships that could have appeared to influence the work reported in this paper.

Acknowledgments

This work was supported by the National Key

R&D Program of China (Nos. 2023YFC3904202, 2022YFC2904500), and Major Science and Technology Program of Yunnan Province, China (No. 202202AB080012).

References

[1] HAN Ji-kang, CHEN Peng, LIU Tai-shan, LI Yan-feng. Research and application of fluidized flotation units: A review [J]. Journal of Industrial and Engineering Chemistry, 2023, 126: 50−68.

[2] JELDRES R I, FORBES L, CISTERNAS L A. Effect of seawater on sulfide ore flotation: A review [J]. Mineral Processing and Extractive Metallurgy Review, 2016, 37(6): 369−384.

[3] PITA F A. True flotation and entrainment of kaolinitic ore in batch tests [J]. Mineral Processing and Extractive Metallurgy Review, 2015, 36(4): 213−222.

[4] ZHOU You, ALBIJANIC B, TADESSE B, WANG Yu-ling, YANG Jian-guo. Investigation of bubble-particle attachment interaction during flotation [J]. Minerals Engineering, 2019, 133: 91−94.

[5] CAO Fei, SUN De-si, QIU Xian-hui, ZHOU De-zhi, ZHANG Xing-rong, SUN Chuan-yao. Synthesis of novel thionocarbamate for copper−sulfur flotation separation and its adsorption mechanism [J]. Transactions of Nonferrous Metals Society of China, 2022, 32(8): 2709−2718.

[6] JIA Xiao-dong, SONG Kai-wei, CAI Jin-peng, SU Chao, XU Xiao-huui, MA Yin-yu, SHEN Pei-lun, LIU Dian-wen. Effect of oxygen and sodium sulfide on flotation of cuprite and its modification mechanism [J]. Transactions of Nonferrous Metals Society of China, 2023, 33(4): 1233−1243.

[7] NEWCOMBE B, BRADSHAW D, WIGHTMAN E. Flash flotation ... and the plight of the coarse particle [J]. Minerals Engineering, 2012, 34: 1−10.

[8] KROMAH V, POWOE S B, KHOSRAVI R, NEISIANI A A, CHELGANI S C. Coarse particle separation by fluidized-bed flotation: A comprehensive review [J]. Powder Technology, 2022, 409: 117831.

[9] DAI Zong-fu, FORNASIERO D, RALSTON J. Particle-bubble collision models—A review [J]. Advances in Colloid and Interface Science, 2000, 85(2/3): 231−256.

[10] TAO D. Role of bubble size in flotation of coarse and fine particles—A review [J]. Separation Science and Technology, 2005, 39(4): 741−760.

[11] ASAMOAH R K, SKINNER W, ADDAI-MENSAH J. Alkaline cyanide leaching of refractory gold flotation concentrates and bio-oxidised products: The effect of process variables [J]. Hydrometallurgy, 2018, 179: 79−93.

[12] CURRY J A, ISMAY M J L, JAMESON G J. Mine operating costs and the potential impacts of energy and grinding [J]. Minerals Engineering, 2014, 56: 70−80.

[13] JAMESON G J, COOPER L, TANG K K, EMER C. Flotation of coarse coal particles in a fluidized bed: The effect of clusters [J]. Minerals Engineering, 2020, 146: 106099.

[14] KOHMUENCH J N, MANKOSA M J, THANASEKARAN H, HOBERT A. Improving coarse particle flotation using the HydroFloat™ (raising the trunk of the elephant curve) [J]. Minerals Engineering, 2018, 121: 137−145.

[15] XU D, AMETOV I, GRANO S R. Quantifying rheological and fine particle attachment contributions to coarse particle recovery in flotation [J]. Minerals Engineering, 2012, 39: 89−98.

[16] GONTIJO C, FORNASIERO D, RALSTON J. The limits of fine and coarse particle flotation [J]. Canadian Journal of Chemical Engineering, 2007, 85(5): 739−747.

[17] DICKINSON J E, GALVIN K P. Fluidized bed desliming in fine particle flotation − Part I [J]. Chemical Engineering Science, 2014, 108: 283−298.

[18] YIN Wan-Zhong, WANG Ji-Zhen. Effects of particle size and particle interactions on scheelite flotation [J]. Transactions of Nonferrous Metals Society of China, 2014, 24(11): 3682−3687.

[19] FOSU S, AWATEY B, SKINNER W, ZANIN M. Flotation of coarse composite particles in mechanical cell vs. the fluidised-bed separator (The HydroFloat™) [J]. Minerals Engineering, 2015, 77: 137−149.

[20] ALBIJANIC B, OZDEMIR O, HAMPTON M A, NGUYEN P T, NGUYEN A V, BRADSHAW D. Fundamental aspects of bubble-particle attachment mechanism in flotation separation [J]. Minerals Engineering, 2014, 65: 187−195.

[21] LI Chao, KANG He, WANG Ai, ZHANG Bo-ai, CAO Yi-jun. Fluidized-bed flotation of coarse molybdenite particles: Matching mechanism for bubble and particle sizes [J]. Separation and Purification Technology, 2023, 324: 124592.

[22] WANG Dong-dong, WANG Huai-fa. Flotation of coarse coal particles in a three-phase gas-solid-liquid fluidised bed [J]. International Journal of Oil Gas and Coal Technology, 2018, 17(2): 222−237.

[23] AWATEY B, THANASEKARAN H, KOHMUENCH J N, SKINNER W, ZANIN M. Optimization of operating parameters for coarse sphalerite flotation in the HydroFloat fluidised-bed separator [J]. Minerals Engineering, 2013, 50/51: 99−105.

[24] AWATEY B, THANASEKARAN H, KOHMUENCH J N, SKINNER W, ZANIN M. Critical contact angle for coarse sphalerite flotation in a fluidised-bed separator vs. a mechanically agitated cell [J]. Minerals Engineering, 2014, 60: 51−59.

[25] JAMESON G J, EMER C. Coarse chalcopyrite recovery in a universal froth flotation machine [J]. Minerals Engineering, 2019, 134: 118−133.

[26] PANJIPOUR R, KARAMOOZIAN M, ALBIJANIC B. Investigations of gas holdup, interfacial area of bubbles and bubble size distributions in a pilot plant flotation column [J]. Minerals Engineering, 2021, 164: 106819.

[27] XU Hong-xiang, LIU Jiong-tian, LI Xiao-bing, ZHANG Chun-juan, WANG Yong-tian. The effect of bubble size on oil-water separation efficiency for a novel oil-water separation column [J]. Separation Science and Technology, 2016, 51(1): 41−48.

[28] NI Chao, BU Xiang-ning, XIA Wen-cheng, PENG Yao-li, XIE Guang-yuan. Effect of slimes on the flotation recovery and kinetics of coal particles [J]. Fuel, 2018, 220: 159−166.

[29] ZHANG Wei. Evaluation of effect of viscosity changes on bubble size in a mechanical flotation cell [J]. Transactions of Nonferrous Metals Society of China, 2014, 24(9): 2964−2968.

[30] ZHU Hong-zheng, VALDIVIESO A L, ZHU Jin-bo, MIN Fan-fei, SONG Shao-xian, ARROYO M A C. Air dispersion and bubble characteristics in a downflow flotation column [J]. Mineral Processing and Extractive Metallurgy Review, 2019, 40(3): 224−229.

[31] FILIPPOV L O, JAVOR Z, PIRIOU P, FILIPPOVA I V. Salt effect on gas dispersion in flotation column-bubble size as a function of turbulent intensity [J]. Minerals Engineering, 2018, 127: 6−14.

[32] GUPTA A K, BANERJEE P K, MISHRA A, SATISH P, PRADIP. Effect of alcohol and polyglycol bubble size and ether frothers on foam stability, bubble size and coal flotation [J]. International Journal of Mineral Processing, 2007, 82(3): 126−137.

[33] DUINEVELD P C. Bouncing and coalescence of two bubbles in pure water [J]. Journal of Fluid, 1995, 31: 151−160.

操作参数对粗颗粒浮选柱中气泡尺寸及分布的影响

晋应升[1]，孙伟[1]，彭建[1]，沈政昌[2]，韩海生[1]，孙磊[1]，肖遥[1]，罗远家[1]，陈毅[1]

1. 中南大学 资源加工与生物工程学院，长沙 410083；
2. 北京矿冶科技集团有限公司 矿物加工科学与技术国家重点实验室，北京 100070

摘　要：采用高速摄影仪动态测量系统对实验室规模的粗颗粒浮选柱内气泡尺寸及分布进行试验研究。考察表观水速、表观气速和起泡剂用量等操作参数对气泡尺寸及分布特性的影响。该研究旨在为粗颗粒浮选柱内流态化浮选的研究提供理论支持。结果表明，采用高速射流经过喉管可产生负压，吸入空气并形成气泡，自然吸气状态下气液比为 1:3~1:2.5 时，气泡数最多。增大充气量可使气泡直径分布从尖峰状变为平缓峰。此外，添加起泡剂可以缩小气泡大小分布的范围。气泡 Sauter 直径与表观气速呈显著正相关，与表观水速和起泡剂浓度呈负相关。

关键词：粗颗粒浮选；流态化浮选；气泡尺寸；表观水速

(Edited by Xiang-qun LI)